JOURNAL OF SPACECRAFT AND ROCKETS
Vol. 31, No. 1, January–February 1994

Characteristics of the Shuttle Orbiter Leeside Flow During a Re-Entry Condition

William L. Kleb* and K. James Weilmuenster†
NASA Langley Research Center, Hampton, Virginia 23681

A study of the leeside flow characteristics of the Shuttle Orbiter is presented for a re-entry flight condition. The flow is computed using a point-implicit, finite-volume scheme known as the Langley aerothermodynamic upwind relaxation algorithm (LAURA). LAURA is a second-order-accurate, laminar Navier-Stokes solver incorporating finite-rate chemistry with a radiative equilibrium wall temperature distribution and finite-rate wall catalysis. The computational results are compared with measured inflight surface pressure and surface heating from several Shuttle Orbiter flights. In addition, a leeside surface temperature distribution is compared with a surface temperature distribution derived from the Shuttle infrared leeside temperature sensing (SILTS) flight experiment.

Nomenclature

B = semispan of the wing, m
C = local chord of the wing, m
h = altitude, km
L = reference length, m
M_∞ = freestream Mach number
P_∞ = freestream pressure, Pa
q = heat flux, W/cm^2
q_0 = reference heat flux, W/cm^2
Q = freestream dynamic pressure, Pa
T = temperature, K
T_0 = reference temperature, K
V_∞ = freestream velocity, m/s
X = distance along the longitudinal axis, m
Y = distance along the pitch axis, m
α = angle of attack, deg
β = yaw angle, deg
Γ_n = atomic nitrogen recombination coefficient
Γ_O = atomic oxygen recombination coefficient
ϵ = emissivity
ρ_∞ = freestream density, kg/m^3
σ = Stefan-Boltzmann constant W/cm^{2}K^4
Φ = meridional angle, deg

Introduction

DURING the design of lifting-body configurations such as the HL-20, Hermes, Hope II, Buran, etc., the harsh environment during re-entry dictates a significant challenge of coping with the associated high heating rates on the windward surfaces. As a result, the windward aerothermal environment has been extensively studied and is fairly well understood. Correspondingly, the thermal protection system (e.g., reusable tiles) can be designed rather efficiently with regard to both safety and weight requirement since the windward heating environment is reasonably well defined. The leeside heating environment on the other hand has not been studied in great depth. Whereas extremely high heating rates are not commonplace on the leeward side of the vehicle, the flow physics remains largely unexplored. This vague knowledge of the leeside flowfield has led to conservative thermal protection system designs for this part of the vehicle which implies that a significant weight penalty is being imposed on the vehicle.

The inability of ground-test facilities to reproduce the high-energy flows present during re-entry conditions, coupled with the prohibitive expense of flight tests, leads to the use of analytic methods to describe the flow. Several previous efforts have been made to compute complex vehicle flowfields for re-entry speeds for various conditions.[1–16] Founded on the principles developed by Kutler et al.,[1] the supersonic/hypersonic, three-dimensional, external, inviscid (STEIN) flow code of Marconi et al.[2] was among the first to treat a Shuttle-like configuration using inviscid analysis. Shortly thereafter, Schiff and Steger[3] introduced the subsonic sublayer approximation for the parabolized Navier-Stokes (PNS) equations. This enabled stable space marching of the PNS equations along a body. PNS work was continued by Li,[4,5] which consisted of a re-entry flow around the Shuttle-like vehicle, incorporating "real" gas effects. Venkatapthy et al.[6] used the PNS formulation to compare with wind-tunnel data for the Orbiter. This work was followed by Szema et al.,[10] who computed a re-entry flight condition for a Shuttle-like configuration. Balakarishnan[7] presented a zero angle of attack, high Mach number condition, incorporating real gas effects. Prabhu and Tannehill[8] computed a re-entry flight condition for the Shuttle Orbiter and compared it with flight data. Meanwhile, the more computer-memory intensive Euler equation solvers were also being developed and applied to Shuttle-like vehicles at high speeds.[9–13] More recently, sufficient computational power has enabled the solution of the full or thin-layer Navier-Stokes equations over complex re-entry vehicles to be computed, including finite-rate chemistry.[14–16]

A limited amount of flight data are available for the Shuttle Orbiter. For the first five space transportation system flights (STS-1–5) of the Shuttle Orbiter Columbia, the vehicle was instrumented to measure surface pressures and temperatures. This instrumentation is known as the developmental flight instrumentation (DFI). The surface temperatures and related heating rates are given by Hartung and Throckmorton.[17–19] In addition, on subsequent flights of Shuttle Orbiter Columbia, the Shuttle infrared leeside temperature sensing (SILTS) experiment[20] provides a map of the surface temperatures over portions of the leeside surface of the vehicle.

This paper makes comparisons with available flight data for the Shuttle Orbiter and provides some insight into the intricate leeside flow structures during re-entry. This flowfield analysis serves to assess the ability of the computational models within the Langley aerothermal dynamic upwind relaxation algorithm (LAURA) to predict the leeside environment through examining not only the leeside pressures and heating rates but also through a detailed

Presented as Paper 92-2951 at the AIAA 27th Thermophysics Conference, Nashville, TN, July 6–8, 1992; received Sept. 24, 1992; revision received Feb. 19, 1993; accepted for publication Feb. 19, 1993.

*Research Engineer, Aerothermodynamics Branch, Space Systems Division.

†Senior Research Engineer, Aerothermodynamics Branch, Space Systems Division. Associate Fellow AIAA.

comparison of the temperature distributions predicted for the leeside of the wing as compared with SILTS flight data.

Shuttle Geometry

The actual Shuttle Orbiter geometry is shown in Fig. 1. Since the complexity of the aft portion represents a difficult volumetric grid construction problem, it was simplified for the purposes of this investigation. These simplifications consisted of removing the tail surface, engine nozzles, and body flap while continuing the wing's elevon hinge-line edge thickness as a solid surface extending to the outflow plane. Figure 2 shows the simplified geometry. For the high Mach number and angle-of-attack flow being studied, the shock layer is predominately an inviscid, supersonic flow. Thus the influence of the simplifications should be localized and, in particular, should not influence the flow over the leeside of the vehicle.

The computational mesh was constructed in several phases. First, a surface mesh was generated on the simplified geometry using the GRIDGEN package.[21] Based on this grid distribution and conservative estimates of the outer boundary location, GRIDGEN was used to generate surface meshes on the remaining boundary faces of the computational domain (the upper and lower symmetry planes, the outflow plane, and the outer boundary). Since all of the faces of a "computational cube" had now been defined, the algebraic volume grid generation within GRIDGEN was used to generate the interior points. This algebraic volume grid was then smoothed using the Poisson solver within GRIDGEN, specifying that grid lines should be normal to the body surface and symmetry planes.

The final computational mesh is comprised of just over 1×10^6 grid points with 121 points distributed streamwise along the body, 101 points circumferential, and 91 points between the body and just outside the bow shock (i.e., in the uniform, freestream flow). Figure 3 shows two details (planform and frontal views) of the surface mesh, whereas Fig. 4 depicts selected planes of the volume mesh (with every other grid line perpendicular to the body-normal direction removed for visual clarity).

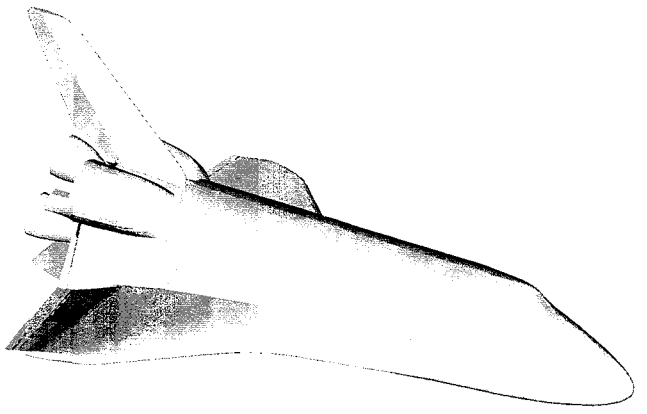

Fig. 1 Shuttle Orbiter surface definition.

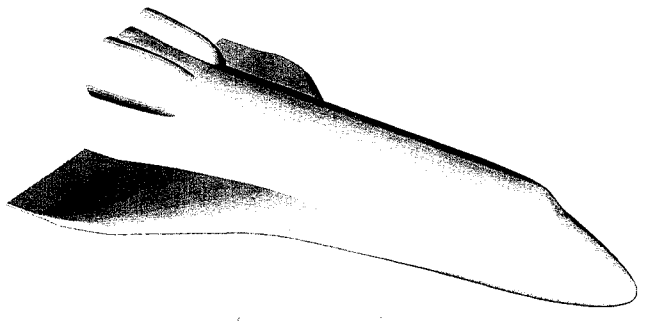

Fig. 2 Simplified Shuttle Orbiter surface definition.

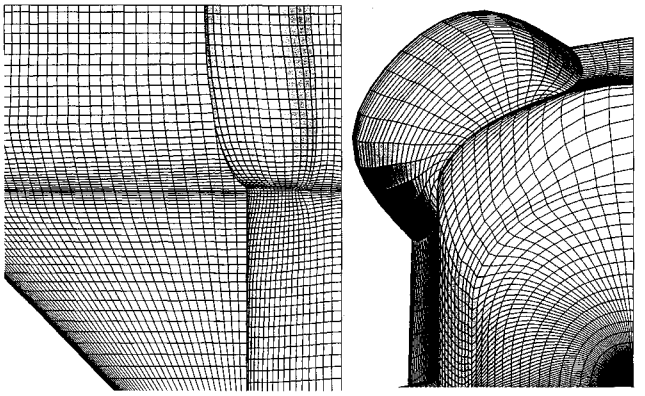

Fig. 3 Planform and frontal details of the surface mesh.

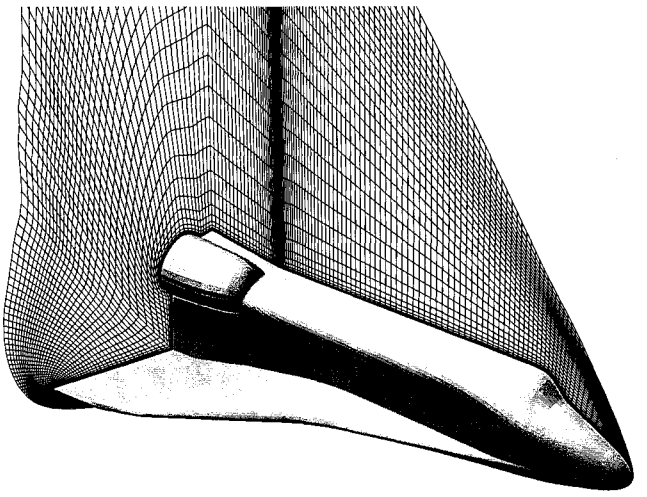

Fig. 4 Partial view of volume grid; every other line perpendicular to the body-normal direction omitted for clarity.

Numerical Method

The LAURA code is a point-implicit, finite-volume solver based on the upwind-biased flux difference splitting of Roe.[22] The scheme utilizes Yee's symmetric total variation diminishing discretization[23] to achieve second-order spatial accuracy while incorporating Harten's entropy flux.[24] LAURA is capable of modeling both Euler and laminar Navier-Stokes flow for a host of different air chemistry assumptions: perfect gas, equilibrium, chemical nonequilibrium, and thermochemical nonequilibrium. For this computation, LAURA was primarily run in thin-layer, laminar Navier-Stokes mode with chemical nonequilibrium. Specific details of the basic algorithm can be found in Ref. 25.

LAURA provides for automatic grid adaptation to the flowfield after an initial solution is generated. This automatic redistribution of points plays the delicate balance of providing proper spacing near the wall to resolve the boundary layer, clustering points in the vicinity of the bow shock, and providing a minimum number of points outside of the bow shock structure, i.e., that portion of the computational domain where freestream conditions prevail. This form of adaptation not only allows for a highly efficient use of the limited number of grid points available due to computer memory restrictions but also provides better resolution of the strong bow shock by aligning the computational cells with the shock gradients.

For the altitude and velocity of the flight point considered in this study, it has been shown by Hartung and Throckmorton[26] that the flow over the Shuttle Orbiter is still laminar. Furthermore, the thin-layer assumption (neglecting viscous terms tangential to the body surface) is used for two reasons: 1) reduction of computational resources used (both memory and CPU time) and 2) as outlined by Baldwin and Lomax[27] there is generally not sufficient grid resolu-

tion to resolve the streamwise gradients if they were to become significant to the viscous energy momentum balance. The effect of neglecting these terms is discussed in a later section of the paper.

Aerothermodynamic Models

Some of the major considerations, specific to this flowfield application are presented next. Extensive details of the aerothermodynamic models used in the LAURA code can be found in Ref. 28.

Finite-Rate Chemistry

The flowfield chemistry is described by the kinetic model of Park[29] with modifications for the dissociation rates according to Ref. 30. However, two simplifying assumptions were used for this case: 1) collapsing the two-temperature model into a single temperature and 2) using only 7 of the proposed 11 species.

The first assumption is physically valid because the postshock temperatures of this flow are relatively low (≈6500 K), and thus the vibrational, translational, rotational, and electronic energy modes are near equilibrium. The seven species accounted for in this calculation are O_2, N_2, O, N, NO, NO^+, e^-. Again, due to the relatively low-energy level of the flow, ionization of nitrogen and oxygen would be insignificant if included. (This assumption has been reaffirmed by Hartung and Hassan through use of an approximate method described in Ref. 31.)

Finite-Rate Wall Catalysis

Zoby et al.'s[32] and Scott's[33] finite-rate wall catalysis curve fits were used to model the wall catalysis of the Shuttle's reaction-cured-gas coated tiles. Figure 5 shows a plot of atomic recombination coefficients with respect to temperature for oxygen[32] and nitrogen.[33] The validity ranges for both fits are also shown on the plot. Limited data for the lower temperature ranges are available from Refs. 34–36 which show a trend very similar to that given when the curves of Refs. 32 and 33 are extrapolated to the temperature levels found on the leeside of the vehicle. The latter method was chosen for the present study to simplify the model and limit the computational expense of computing the wall catalysis.

In addition to this simplification of the wall catalysis recombination rates, all surfaces of the Shuttle [i.e., all types of reusable tile and other surface insulation, including the reinforced carbon-carbon (RCC) found on the leading edge surfaces] were assumed to follow this trend.

Variable Wall Temperature Distribution

The Stefan-Boltzmann relation was used to compute radiation equilibrium wall temperature distributions from the computed heating rates. This relation links the emissivity of a surface ϵ (the ability to emit radiation compared with a Planck black body) with the heating rate q of that surface,

$$q = \sigma \epsilon T^4$$

where σ is the Stefan-Boltzmann constant (5.67×10^{-8} W/m^{2}K^4).

The emissivities are a function of temperature and surface type as given by Refs. 17–19. The surface of the Shuttle is composed of many disparate materials, and for this study, surfaces were considered as being either dark- or light-colored for determining which set of emissivity functions to use.

Using the relations for emissivities and the Stefan-Boltzmann relation, a wall temperature T at each cell face for the Shuttle surface can be determined from the predicted heating rate q. This iterative process is continued until neither the predicted heating rates nor the inferred wall temperature distribution are changing significantly (≈10 K).

From the analysis of the Shuttle flight data[17–19] at the flight times used in this study, differences of up to 20% are observed between the computed radiated heat flux and the actual computed heat flux. At the low leeside surface temperatures, this difference translated into a 10–20 K difference from the measured temperature at the wall.

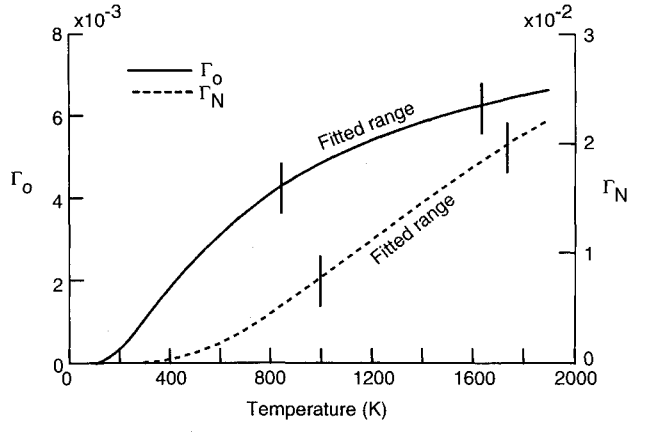

Fig. 5 Atomic recombination coefficients for oxygen and nitrogen as a function of temperature.

Flight Data

As part of the design confirmation procedure for the Shuttle, the DFI was installed on the Orbiter Columbia for the first five flights. Among these instruments were some 200 thermocouples and pressure transducers distributed over the vehicle surface. The measured surface temperatures and computed heating rates for those flights are taken from Refs. 17–19, whereas the flight surface pressures have been extracted from the DFI data base. The accuracy of the surface temperatures and heating rates is addressed in Refs. 17–19. As a result of a number of factors, it is difficult to assign an accuracy to the surface pressure measurements. However, measured flight surface pressures have been shown[9,37] to be in reasonably good agreement with wind-tunnel data and other computational results.

The SILTS data represents high-spatial resolution of the temperature measurements of the leeside surfaces.[20,38] An infrared camera was mounted in a pod at the top of the vertical tail, and it provided a thermal map of the aft portion of the fuselage and the wing. From these images and knowledge of the Orbiter's surface properties, the surface temperatures could be determined. For the SILTS flight used in this study, i.e., STS-28 and -32, only a small contingent of the original DFI thermocouples on the leeside of the vehicle remained operational. The DFI temperature and heating data for these flights were obtained using the same methods as outlined in Refs. 17-19.

Results and Discussion

The computational resources required for this study are discussed. A description of the flight conditions used for comparison is then provided. Next, the salient features of the leeside flow are given. Comparisons of predicted and measured surface quantities (pressures, temperatures, and heating rates) are presented.

Table 1 Matched flight conditions

Quantity	STS-2	STS-3	STS-5	STS-28	STS-32
UTC,[a] s	75,620	56,588	51,120	47,716	33,166
h, km	69.2	72.9	72.4	73.2	72.8
M_∞	24.3	22.2	23.6	24.3	24.4
V_∞, km/s	6.92	7.01	6.83	7.01	7.01
T_∞, K	202	248	209	210	207
P_∞, Pa	3.33	3.76	3.35	3.40	3.32
ρ_∞, kg/m^3 $\times 10^{-5}$	5.75	5.65	5.59	5.28	5.59
α, deg	39.4	39.5	40.3	39.4	40.0
β, deg	−0.3	−0.1	0.2	—[b]	—[b]
Bank, deg	57	64	−64	−66	−71

[a]Universal coordinated time. [b]Not available.

Computational Resources

Using the methods described by Weilmuenster and Gnoffo,[39] the Shuttle Orbiter grid was cut into four streamwise sections. The sections varied between 35 and 45 cells in the streamwise direction, and a typical run would require approximately 70 Cray-2 hours and 100 MW of memory. This time includes running on the initial grid, aligning the grid, and converging the temperature distribution for each block. After the four sections were converged, all four were put back together into one entire grid and run for an additional 50 Cray-2 hours. For this latter run, the code was altered so that it could fit within 125 MW of memory at the expense of efficiency.

Flight Conditions

A flight trajectory point was chosen so that both DFI data (primarily STS flights 2, 3, and 5) and the SILTS data (STS flights 28 and 32) would be available for comparison. An early trajectory time was used so that the flow over the Shuttle Orbiter would be laminar, but the altitude was low enough (≈70 km) for the continuum assumption to be plausible (Knudsen numbers ≈ 0.05). The freestream velocities and densities were matched for five flights: STS-2, -3, -5, -28, and -32. Table 1 shows the freestream conditions for the matched trajectory point. The freestream conditions of STS-28 were used for the numerical simulation of this study.

Flow Structure

Figure 6 shows a computer-simulated, oil-flow representation of the leeside portion of the Shuttle. The figure clearly depicts many of the predicted separation and reattachment lines on the vehicle. Starting from the leading edge of the wing and working around to the top portion of the vehicle, they are as follows:

1) There is a region of very low pressure/density due to rapid expansion of the flow around the wing tip (i.e., the wing-tip vortex), and the corresponding crossflow shock is shown by the abrupt change in flow direct just inboard of the wing tip.

2) Next is a separation line running just behind the leading edge of the wing strake and continuing through the aft wing section caused by a standing shock triggered by the rapid expansion around the strake leading edge (i.e., the wing strake vortex).

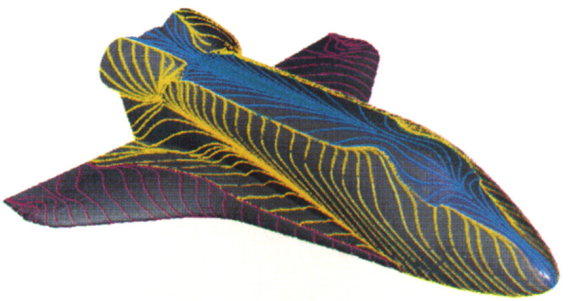

Fig. 6 Computer-simulated oil flow on the leeside of the Shuttle Orbiter.

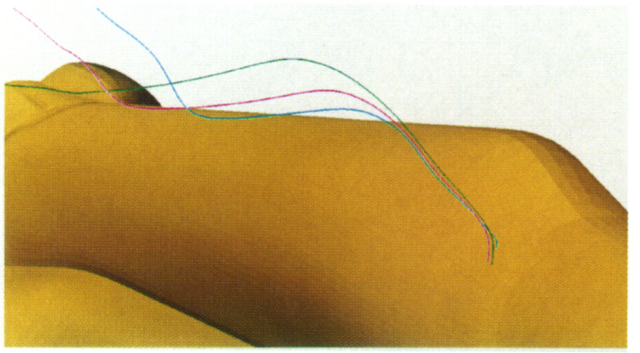

Fig. 7 Streamlines originating just ahead of the canopy.

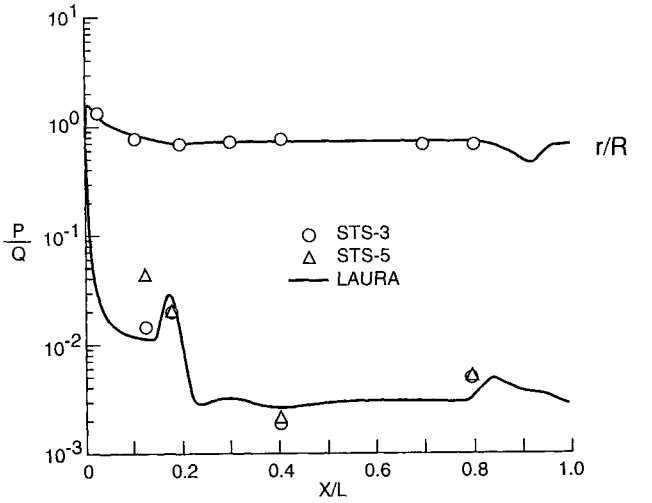

Fig. 8 Windward and leeward centerline pressure comparisons.

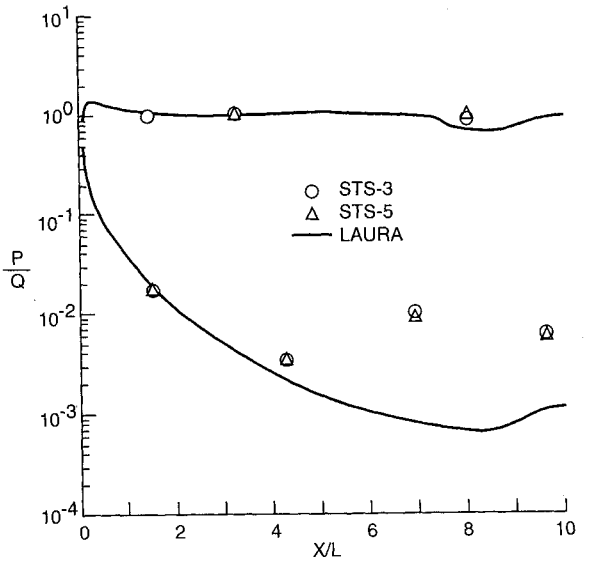

Fig. 9 Pressure distribution comparison for wing station $2Y/B = 0.60$ as a function of chord.

3) A reattachment/shear line follows located diagonally from the beginning of the wing strake to the leading portion of the orbital maneuvering system (OMS) pods.

4) There is a stagnation region just ahead of the OMS pods.

5) Next is a separation line along the upper portion of the body attributed to the standing crossflow shock which serves to turn the flow parallel to the symmetry plane.

6) A smaller separation line on the aft portion of the OMS pods follows due to the crossflow shock.

7) Last is a recirculation region just ahead of the canopy created by the canopy shock.

Figure 7 shows particle traces which originate from just ahead of the canopy. Note that the flow from the recirculation region just ahead of the canopy (Fig. 6) separates and reattaches over the top section of the aft fuselage. The implication of this predicted flow structure will become evident in the discussion of the aft fuselage heating rates.

Surface Pressures

As shown in Fig. 8, comparisons were made with DFI flight data for the windward and leeward centerline pressures. The windward centerline pressures are in excellent agreement. Toward the aft end of the vehicle (from approximately $X/L = 0.93$, aft) the computational model does not accurately model the rear portion of

the vehicle, and thus the dramatic drop and consequent rise in pressure is not physical. The leeward centerline pressures show good comparison with the limited amount of flight data.

Figure 9 shows the pressure distribution at the 60% semispan wing station ($2Y/B = 0.6$) as a function of nondimensionalized chord position (X/C). The elevon hinge line occurs at $X/C = 0.7$ for this semispan station, and the corresponding deviation can be seen in the predicted lower surface pressures due to the nonphysical modeling of the aft portion of the wing. The leeward pressures compare favorably until approximately the 50% chord position. Aft of this point, the flight data are higher than predicted. The effect of the elevon deflection might be suspected for this discrepancy, but for STS-3 and -5 the elevon's were deflected differently (downward 1.7 and 3.7 deg, respectively). This discrepancy between predicted and measured pressures is apparently due to bleedthrough from the gap between the inboard and outboard elevon. This gap is approximately 18 cm (7 in.) wide and occurs just inboard of this wing semispan station. Since this gap was not modeled for the computational solution, the corresponding increase in pressure due to bleedthrough from the windside is not present.

Figure 10 shows the pressure distribution at the 10% fuselage station ($X/L = 0.1$). The meridional angle Φ is measured from the leeward symmetry plane around to the windward symmetry plane. The figure also includes a half-section depiction of the fuselage at the $X/L = 0.1$ station. At this location, the predicted and measured pressures agree very well. Because of sparse pressure data for the leeside, no direct comparison can be made for the top of the fuselage. The trend of the predicted pressures, however, is as expected for a blunt-nosed vehicle at moderate angle of attack, showing a rapid expansion and subsequent recompression while approaching the symmetry plane.

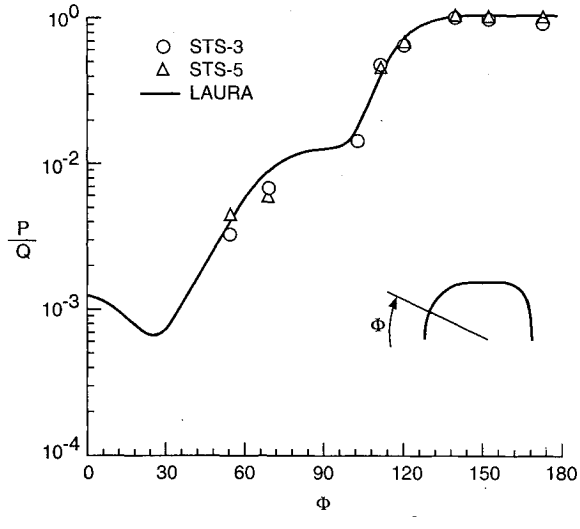

Fig. 10 Cross-sectional pressure comparison at fuselage station $X/L = 0.10$.

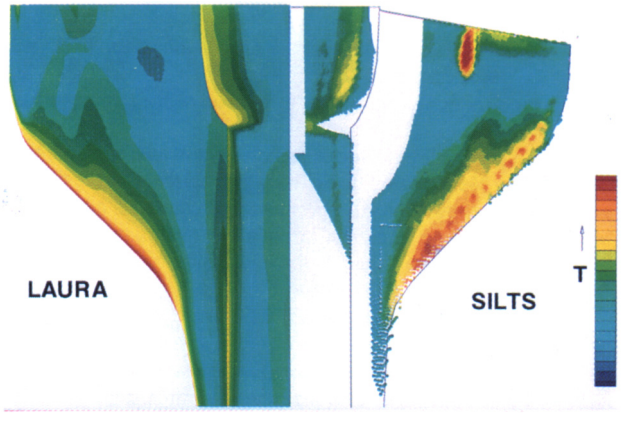

Fig. 11 Leeside wall temperature comparison for the aft end of the Shuttle Orbiter.

Surface Temperatures

Figure 11 is a side-by-side comparison of the leeside wall temperature distribution for the aft portion of the Shuttle. The computed results from LAURA are shown on the left-hand side, and the measured temperatures from the STS-32 SILTS flight are shown on the right-hand side. The SILTS image for STS-28 flight point is nearly identical to STS-32 results, therefore only the one comparison is presented. Recall that the LAURA temperatures are determined from the radiative equilibrium assumption just dis-

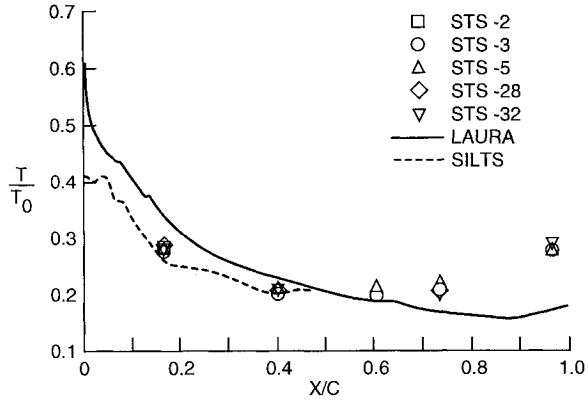

a) Wing station $2Y/B = 0.40$

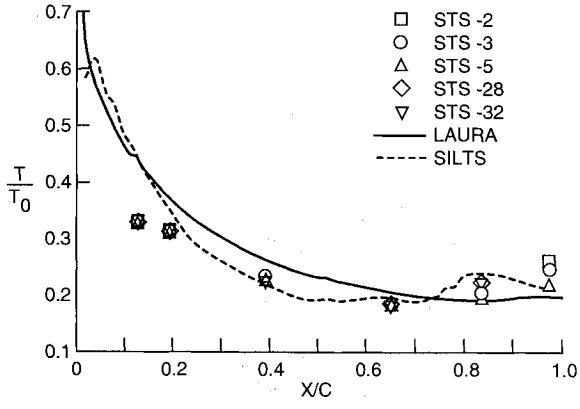

b) Wing station $2Y/B = 0.60$

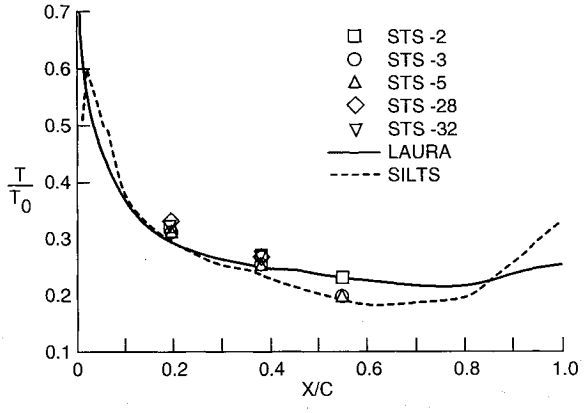

c) Wing station $2Y/B = 0.75$

Fig. 12 Temperature distribution comparisons at various wing semispan stations as a function of chord.

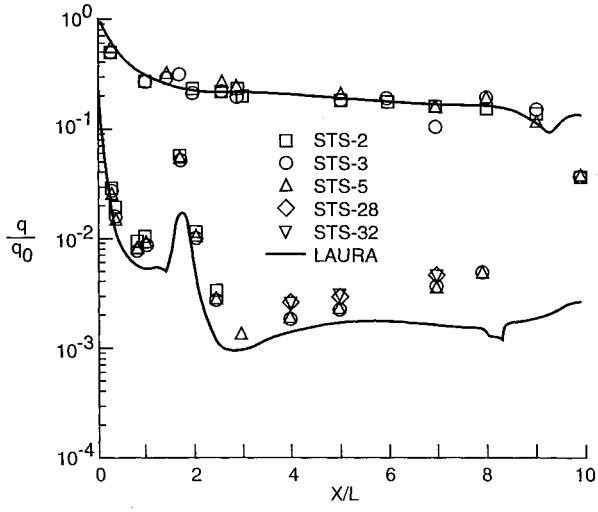

Fig. 13 Windward and leeward centerline heating rate comparisons.

cussed. This equilibrium assumption neglects the effects of the time dependent terms such as conduction.

The figure shows a band of high temperature along the leading edge of the wing as expected. The spotted nature along the forward section of the wing shown in the SILTS image is due to temperature variations across each of the hollow RCC segments which comprise the leading edge. This phenomenon is largely due to the reradiation from the windward surface of the hollow RCC leading-edge sections through to the leeward surface (see Ref. 38). Also depicted by both methods is a streamwise streak of high temperature at approximately 60% of the wing semispan. This corresponds to the wing-bow shock interaction. In addition, both images show areas of low temperature located just under the wing-tip vortex, below the inboard wing-strake vortex structure, and just ahead of the OMS pods. The SILTS image shows a streak of high heating where the windward flow comes through the elevon-elevon gap at the trailing edge of the wing. The computational Shuttle model did not model this gap. The rise in heating on the leading edge of the OMS pods is clearly depicted by both methods. Also of interest is that even though the tail was neglected from the computational model of the Shuttle Orbiter, the temperature distributions are remarkably similar on the top of the fuselage, just ahead of the OMS pod location.

Figure 12 shows the wing upper surface, nondimensionalized temperature distribution as a function of nondimensionalized chord position for three semispan stations ($2Y/B$): 0.40, 0.60, and 0.75. Each sub-figure includes DFI thermocouple data, SILTS data, and the temperature profile predicted by LAURA. The SILTS data for these plots were extracted from the image data shown in Fig. 11. The extracted SILTS data had to be stretched to properly register the leading and trailing edges. This is due to uncertainties in the optical transformations used to obtain the planform image as discussed in Ref. 38. In addition, the reader is cautioned that the aft portion of the LAURA solutions are not physical since the wing was not modeled accurately beyond the elevon hinge line.

The 40% semispan station (Fig. 12a) shows that both sets of flight temperature data are lower than the LAURA prediction. This might be due to conduction along the RCC leading edge which was not computationally modeled. At the 60% semispan station (Fig. 12b), the temperatures predicted by LAURA and the flight measurements are in very good agreement considering the semispan station is very near the wing-bow shock interaction zone. The DFI thermocouple near the leading edge ($X/C = 0.15$), however, is considerably lower than either the SILTS data or the LAURA predictions. At the 70% semispan station (Fig. 12c) the LAURA predictions are within 5% of both sets of flight data.

Surface Heating

Figure 13 shows heating comparisons for the windward and leeward centerlines. The windward centerline values are in very good agreement with all three DFI flights. One isolated discrepancy occurs at the 15% fuselage station ($X/L = 0.15$) where the heating rates shown by the DFI data are nonmonotonic for a short stretch of the vehicle surface. This is attributed to an acoustic microphone which melted on one of the first flights and contaminated a localized downstream area. It should also be noted that several of the tiles on all flights (particularly STS-5) had catalytically enhanced surface.[40] However, as discussed in Ref. 40, the area of influence appears to be very localized and has been omitted in this analysis. The predicted leeward centerline heating rates show a consistently lower trend than the measured flight data, and once past $X/L = 0.55$ not even the trend in heating is captured correctly. The peak heating due to the canopy shock is predicted significantly lower than that measured by flight data. This region is just aft of a bank of four reaction control system (RCS) jets which was not modeled as well as the recessed windows and their associated gap seals. The low predicted heating in this area is of concern because the vortex which originates from just ahead of the canopy reattached along the aft end of the fuselage (refer to Fig. 7). Also, there are not very many grid points in the vicinity of this region (Fig. 3) and the flow may not be adequately resolved.

The heating comparisons at several fuselage cross-sectional stations are shown in Fig. 14. As with the pressure, the meridional angle Φ is measured from the leeward symmetry plane around to the windward symmetry plane, and each sub-figure includes a half-section depiction of the fuselage at the particular station.

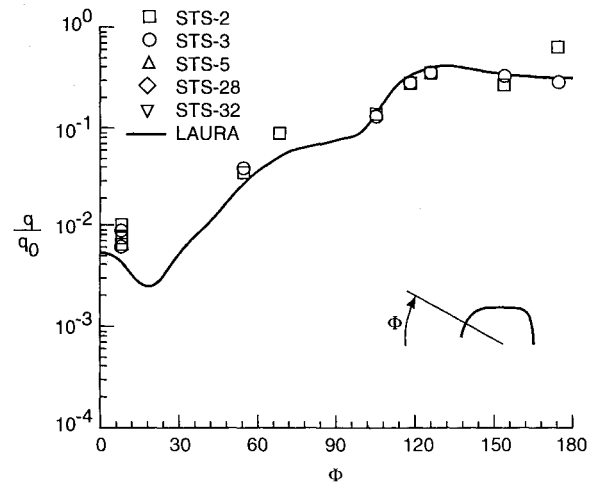

a) Fuselage station $X/L = 0.10$

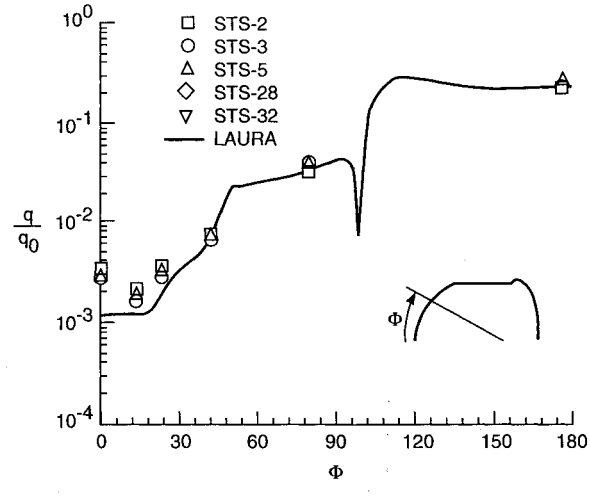

b) Fuselage station $X/L = 0.25$

Fig. 14 Cross-sectional heating comparisons at various fuselage stations along the vehicle. (Fig. cont.)

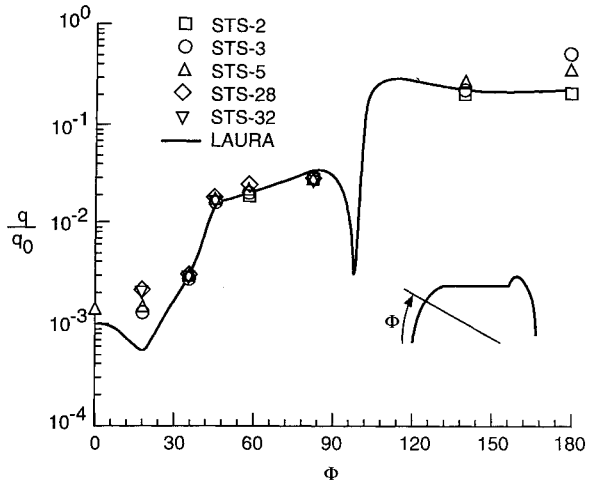

c) Fuselage station $X/L = 0.30$

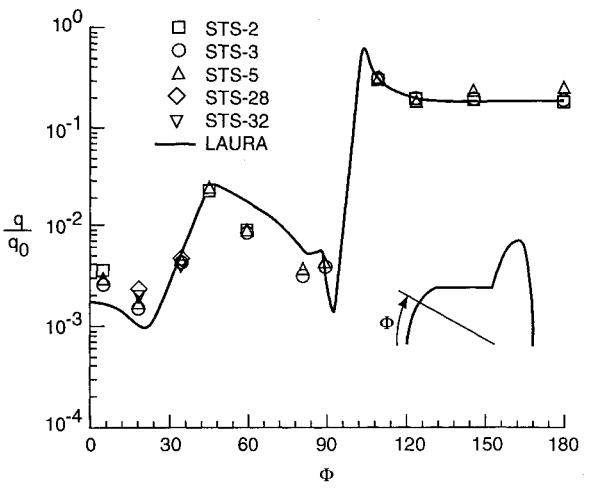

f) Fuselage station $X/L = 0.60$

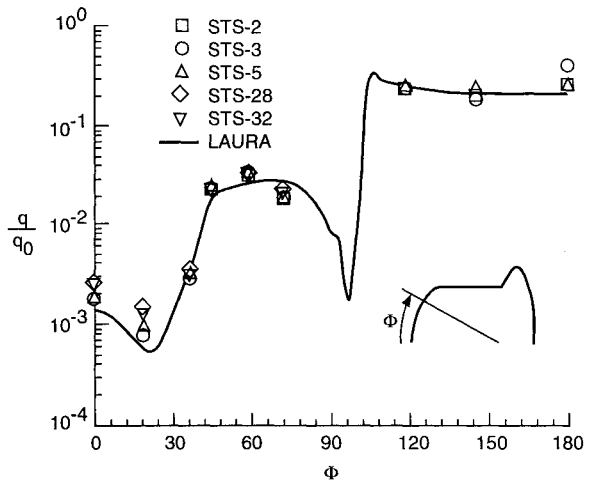

d) Fuselage station $X/L = 0.40$

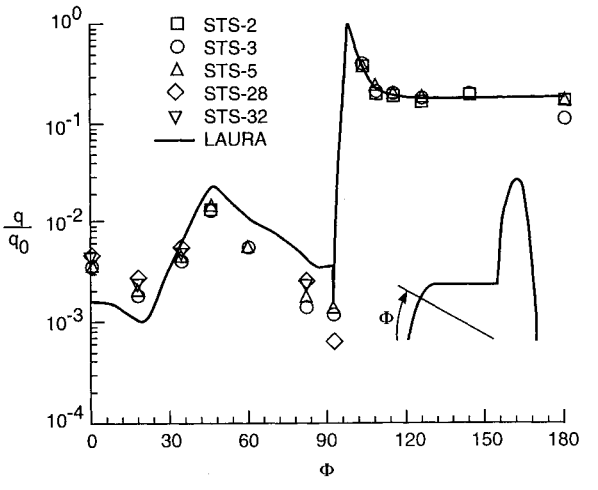

g) Fuselage station $X/L = 0.70$

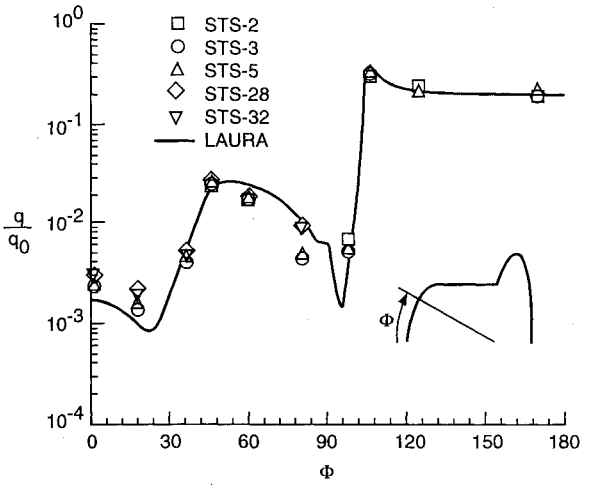

e) Fuselage station $X/L = 0.50$

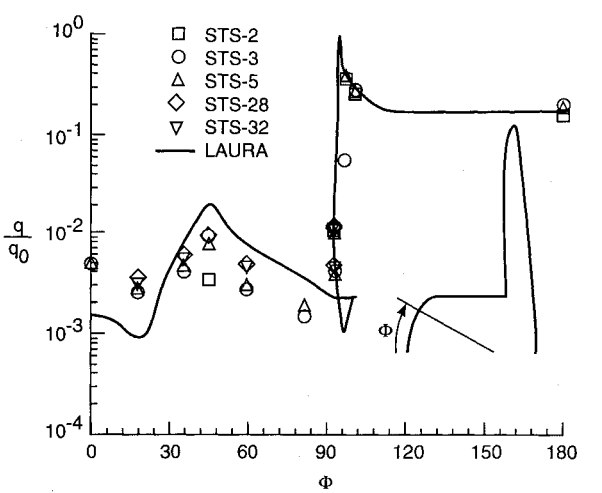

h) Fuselage station $X/L = 0.80$

Fig. 14 (Continued) Cross-sectional heating comparisons at various fuselage stations along the vehicle.

Figure 14a shows the first fuselage station ($X/L = 0.1$). This station is located midway between the cluster of four RCS jets and the beginning of the canopy. The predicted leeward heating rates are somewhat lower than the measured flight data. However, as one approaches the windward surfaces the predicted heating rates show excellent agreement with the flight data.

Figure 14b represents the $X/L = 0.25$ fuselage station which is located just aft of the forward facing windows but still encompasses the swept-back portion of the fuselage, which accommodates the side-facing windows. This stations shows a trend similar to the previous station: underprediction when nearing the leeward centerline but excellent agreement on the sidewall and windward surfaces. At this station, however, the trend of the heating distribution near the leeside centerline is not captured.

Figure 14c ($X/L = 0.3$) is located just aft of the previous station and no longer encompasses the swept-back portion of the fuselage due to the side facing windows. Once again, the windward heating rates agree well, whereas the predicted leeside heating rates are lower than those measured in flight. Again, the trend of the heating rates near the leeside centerline is not properly captured.

Figure 14d depicts the fuselage station at $X/L = 0.4$. At this point, both the windward and leeward heating predictions agree very well with the measured flight data. The predicted heating near the leeside centerline is still slightly lower than the flight data, but the proper trend is now evident.

The next fuselage station ($X/L = 0.5$) is shown by Fig. 14e. As with the previous cross-sectional station, the leeside heating rates are in slight disagreement, but all of the trends are captured. A slight disparity in the flight data is noted at Φ of approximately 75 deg.

The next three sub-figures; 14f, 14g, and 14h show the computed and measured heating rates for fuselage stations of X/L = 0.6, 0.7, and 0.8, respectively. All of these show similar trends: excellent agreement on the windward and side surfaces but overprediction of the heating rates on the upper surface of the wing and underprediction on the lee surface of the fuselage.

General Observations

As a check of the thin-layer Navier-Stokes assumptions, the neglected viscous terms are added in two stages. The first stage is the addition of the circumferential component. The inclusion of this term involves no additional memory and is relatively inexpensive to compute. With this additional term, the changes in the heating rates are highly localized and generally less than 5%. These occur in the wing/bow-shock interaction region, in the vicinity of the wing-tip crossflow shock, and just ahead of the OMS pods. The second stage is to use the full Navier-Stokes equations. This increases the code's memory requirement by approximately 15%, but the computational overhead is no more than 5%. Although the arguments of Baldwin and Lomax[27] indicate that, in general, the effects of the additional terms would be negligible, results demonstrate that in confined regions, the leeside heating rates change by as much as 30%. For example, the heating rates decrease significantly on the fuselage sidewall in the region below the shear line extending between the start of the wing strake and the OMS pad (refer to Fig. 6). This is as might be expected since this is a highly vortical region of the flow. The heating increases by 20% along both crossflow shocks on the wing. Also, a decrease in heating is noted at the front of the OMS pods and along the lower OMS pods/fuselage juncture.

The procedures used to calculate the heating rates from the DFI data[17–19] make assumptions concerning the integrity of the thermocouple/thermal protection material joint. For the flexible materials used throughout the leeside of the Shuttle Orbiter, this is not necessarily a valid assumption. Estimates of error in the procedures outlined in Refs. 17–19 do not include the errors present in the thermocouple measurements themselves. Therefore, considerable unknowns are present in the thermocouple flight data and corresponding heat transfer rates.

Conclusions

A computational solution was presented for a re-entry condition of the Shuttle Orbiter at 40-deg angle of attack for an altitude of 70 km. The initial results demonstrate that the flow structure is quite complex, maintaining several vortical structures, separation lines, shock-shock interaction, and regions of low density flow.

The computed pressures compare well with flight data on the windward and leeward centerlines and for a fuselage cross section. The pressures along a wing semispan station also shows good agreement for the windside, but differ considerably on the leeside near the inboard/outboard elevon gap which was not modeled.

The temperature distributions on the leeside of the wing are well predicted by LAURA. The wing-bow shock interaction region is evident as well as the peak heating on the wing leading edge. This offers confidence in accurately predicting the leeside thermal environment for design considerations.

The use of the thin-layer Navier-Stokes assumption for the leeside flow appears to be adequate for the flight condition studied in this paper. The effects of adding the remaining viscous terms produced only localized changes in the heating rates for the leeside flow and had absolutely no effect on the windside of the vehicle. Of course, a grid refinement study is necessary to completely understand these effects.

The heating rates, overall, compare very favorably with those measured by DFI flight data. The heating rates predicted by LAURA for the top of the aft fuselage are considerably lower than that measured by DFI data. It is expected that better resolution of a vortical structure emanating from the canopy region might rectify this.

Acknowledgments

The authors would like to thank Fred Martin of NASA Johnson Space Center, Houston, Texas, and Samir Deshpande of AMD, Hampton, Virginia, for the data bases used to create the final surface meshes; and Steven Alter of Lockheed, Hampton, Virginia, for aiding in the creation of the initial surface and volume grids used for the computation. The authors would also like to thank Peter Gnoffo for his bounty of helpful strategies for running LAURA and Lin Hartung for her help in extracting the pressure and heating data from the Shuttle data tapes.

References

[1]Kutler, P., Reinhardt, W. A., and Warming, R. F., "Multishocked, Three-Dimensional Supersonic Flowfields with Real Gas Effects," *AIAA Journal*, Vol. 11, No. 5, 1973, pp. 657–664; also AIAA Paper 72-702, 1972.

[2]Marconi, F., Sala, M., and Yaeger, L., "Development of a Computer Code for Calculating the Steady Super/Hypersonic Inviscid Flow Around Real Configurations," NASA CR 2675, 1976.

[3]Schiff, L. B., and Steger, J. L., "Numerical Simulation of Steady Supersonic Viscous Flow," NASA TP 1749, May 1981; also AIAA Paper 79-0130, Jan. 1979.

[4]Li, C. P., "Numerical Simulation of Reentry Flow Around the Shuttle Orbiter Including Real Gas Effects," *Computers in Flow Predictions and Fluid Dynamics Experiments*, Nov. 1981, pp. 141–145.

[5]Li, C. P., "Implicit Solution of the Shock-Layer Flow Around General Bodies," *AIAA Journal*, Vol. 20, No. 2, 1982, pp. 175–183; see also AIAA Paper 81-0191, 1981.

[6]Venkatapathy, E., Rakich, J. V., and Tannehill, J. C., "Numerical Solution of Space Shuttle Orbiter Flow Field," AIAA Paper 82-0028, Jan. 1982.

[7]Balakrishnan, A., "Computation of a Viscous Real Gas Flowfield for the Space Shuttle Orbiter," AIAA Paper 84-1748, June 1984.

[8]Prabhu, D. K., and Tannehill, J. C., "Numerical Solution of Space Shuttle Orbiter Flow Field Including Real Gas Effects," AIAA Paper 84-1747, June 1984.

[9]Weilmuenster, K. J., "High Angle of Attack Inviscid Flow Calculations Over a Shuttle-Like Vehicle with Comparisons to Flight Data," AIAA Paper 83-1798, 1983.

[10]Szema, K. Y., Griffith, B. J., Maus, J. R., and Best, J. T., "Laminar Viscous Flow Field Prediction of Shuttle-Like Vehicle Aerodynamics," AIAA Paper 83-0211, Jan. 1983.

[11]Maus, J. R., Griffith, B. J., Szema, K. Y., and Best, J. T., "Hypersonic Mach Number and Real Gas Effects of Space Shuttle Orbiter Aerodynamics," AIAA Paper 83-0343, Jan. 1983.

[12]Balakrishnan, A., Lombard, C. K., and Davy, W. C., "Real Gas Flowfields About Three-Dimensional Configurations," AIAA Paper 83-0581, Jan. 1983.

[13]Stoufflet, B., Periaux, J., Fezoui, F. F., and Dervieux, A., "Numerical Simulation of 3-D Hypersonic Euler Flows Around Space Vehicles Using Adapted Finite Elements," AIAA Paper 87-0560, Jan. 1987.

[14]Wada, Y., and Kubota, H., "Numerical Simulation of Re-Entry Flow around the Space Shuttle with Finite Rate Chemistry," *Proceedings of the Seventeenth International Symposium on Space Technology and Science*, May 1990.

[15]Wada, Y., Ogawa, S., Kubota, H., and Akimoto, T., "Numerical Simulation of Re-Entry Flow Around the Space Shuttle with Finite-Rate Chemistry," *Proceedings of the Seventeenth International Symposium on Space Technology and Science*, May 1990, pp. 719–728.

[16]Yamamoto, Y., "Numerical Simulation of Hypersonic Viscous Flow for the Design of H-II Orbiting Plane (HOPE): Part II," AIAA Paper 91-1390, June 1991.

[17]Hartung, L. C., and Throckmorton, D. A., "Space Shuttle Entry Heating Data Book: Vol. 1—STS-2," NASA RP-1191, May 1988.

[18]Hartung, L. C., and Throckmorton, D. A., "Space Shuttle Entry Heating Data Book: Vol. II—STS-3," NASA RP-1192, May 1988.

[19]Hartung, L. C., and Throckmorton, D. A., "Space Shuttle Entry Heating Data Book: Vol. III—STS-5," NASA RP-1193, May 1988.

[20]Throckmorton, D. A., Zoby, E. V., and Kantsios, A. G., "The Shuttle Infrared Leeside Temperature Sensing (SILTS) Experiment," AIAA Paper 85-0328, Jan. 1985.

[21]Steinbrenner, J. P., Chawner, J. R., and Fouts, C. L., "The GRIDGEN 3D Multiple Block Grid Generation System: Vol. 1—Final Report," WRDC TR 90-3022, July 1990.

[22]Roe, P. L., "Approximate Riemann Solvers, Parameter Vectors, and Difference Schemes," *Journal of Computational Physics,* Vol. 43, Oct. 1981, pp. 357–372.

[23]Yee, H. C., "On Symmetric and Upwind TVD Schemes," NASA TM-88325, 1986.

[24]Harten, A., "High Resolution Schemes for Hyperbolic Conservation Laws," *Journal of Computational Physics,* Vol. 49, Feb. 1983, pp. 357–393.

[25]Gnoffo, P. A., "An Upwind-Biased, Point-Implicit Relaxation Algorithm for Viscous, Compressible Perfect-Gas Flows," NASA TP-2953, Feb. 1990.

[26]Hartung, L. C., and Throckmorton, D. A., "Computer Graphic Visualization of Orbiter Lower Surface Boundary-Layer Transition," *Journal of Spacecraft and Rockets,* Vol. 24, No. 2, 1987, pp. 109–114.

[27]Baldwin, B. S., and Lomax, H., "Thin-Layer Approximation and Algebraic Model for Separated Turbulent Flows," AIAA Paper 78-257, Jan. 1978.

[28]Gnoffo, P. A., Gupta, R. N., and Shinn, J., "Conservation Equations and Physical Models for Hypersonic Air Flows in Thermal and Chemical Nonequilibrium," NASA TP-2867, 1989.

[29]Park, C., "Assessment of Two-Temperature Kinetic Model for Ionizing Air," AIAA Paper 87-574, June 1987.

[30]Park, C., *Nonequilibrium Hypersonic Aerothermodynamics,* Wiley, New York, 1990.

[31]Hartung, L. C., and Hassan, H. A., "Radiation Transport Around Axisymmetric Blunt Body Vehicles Using a Modified Differential Approximation," AIAA Paper 92-0119, Jan. 1992.

[32]Zoby, E. V., Gupta, R. N., and Simmonds, A. L., "Temperature-Dependent Reaction-Rate Expression for Oxygen Recombination at Shuttle Entry Conditions," AIAA Paper 84-0224, Jan. 1984.

[33]Scott, C. D., "Catalytic Recombination of Nitrogen and Oxygen on High-Temperature Reusable Surface Insulation," AIAA Paper 80-1477, 1980.

[34]Kim, Y. C., "Study of the Recombination of Nitrogen and Oxygen Atoms on Surfaces of Materials Used in Space Vehicles: Final Report," Stanford Univ., NCA 2-158, Stanford, CA, Sept. 1986.

[35]Marinelli, W. J., and Campbell, J. P., "Spacecraft-Metastable Energy Transfer Studies: Final Report," NAS 9-17565, July 1986.

[36]Marinelli, W. J., "Collisional Quenching of Atoms and Molecules on Spacecraft Thermal Protection Surfaces," AIAA Paper 88-2667, June 1988.

[37]Bradley, P. F., Siemers, P. M., III, and Pruett, C. D., "Comparison of Forward Fuselage Space Shuttle Orbiter Flight Pressure Data to Wind-Tunnel and Analytical Results in the Hypersonic Mach Number Range," AIAA Paper 81-2477, Nov. 1981.

[38]Throckmorton, D. A., Dunavant, J. C., and Myrick, D. L., "Shuttle Infrared Leeside Temperature Sensing (SILTS) Experiment—STS 28 Preliminary Results," AIAA Paper 90-1741, June 1990.

[39]Weilmuenster, K. J., and Gnoffo, P. A., "Solution Strategies and Heat Transfer Calculations for Three-Dimensional Configurations at Hypersonic Speeds," AIAA Paper 92-2921, July 1992.

[40]Stewart, D. A., Rakich, J. V., and Lanfranco, M. J., "Catalytic Surface Effects Experiment on Space Shuttle," AIAA Paper 81-1143, June 1981.